PAPER

Check for updates

Computational screening of single-atom alloys TM@Ru(0001) for enhanced electrochemical nitrogen reduction reaction†

Gurpreet Kour, Xin Mao and Aijun Du [ID] *

Searching for highly efficient, active, and stable electrocatalysts for the nitrogen reduction reaction is vital to supersede the energy-intensive Haber–Bosch process. The electrocatalytic nitrogen reduction reaction (NRR) is one of the most promising strategies to synthesize value-added ammonia (NH_3) under mild conditions with low energy utilization and less greenhouse gas emission. However, the lack of effective electrocatalysts remains the major hurdle for its practical applications. Ruthenium is generally considered a promising electrocatalyst for the electrochemical NRR. However, it exhibits a high overpotential corresponding to the potential determining step in the reduction pathway. Herein, using density functional theory, we systematically investigated the potential of a series of transition metal-doped Ru-based TM@Ru(0001) (TM = Sc−Zn, Y−Cd) single-atom alloys to evaluate their NRR activity. Among all the studied catalysts, it was found that the V doped Ru(0001) SAA exhibited a reduced kinetic barrier of about 1.14 eV as compared to that of the pure Ru(0001) corresponding to the potential determining step (PDS). In addition, it showed a significantly low negative limiting potential of −0.15 V for the PDS along with thermodynamical stability and high selectivity over the competing hydrogen evolution reaction (HER). The Climbing-Image Nudged Elastic Band (CI-NEB) method was employed to calculate the barrier height between various hydrogenation steps of the reduction reaction followed by the calculation of turnover frequency (TOF) for V@Ru(0001) using a microkinetic modelling approach. The TOF for V@Ru(0001) was found to be 4.24×10^{-3} per s per site at 100 bar and 700 K, which is far better than that of the pure Ru(0001) surface. This report provides a new design strategy to improve the catalytic performance of Ru(0001) for effective NRR.

1. Introduction

Conversion of atmospheric nitrogen (N_2) to ammonia (NH_3), also known as nitrogen fixation, is one of the most significant processes of industries. NH_3 is not only a green energy carrier but also constitutes an important chemical in manufacturing dyes, explosives, medicaments, fertilizers, *etc.*[1] Industrial production of NH_3 primarily relies on the well-known Haber–Bosch process that requires very high temperature (300–500 °C) and high pressure (150–200 atm).[2] However, this process accounts for 2% of the world's annual total energy consumption and liberates enormous amounts of greenhouse gases into the atmosphere. Thus, it is crucial to develop an alternative approach for sustainable and economical ammonia synthesis under mild conditions of temperature and pressure.

Electrocatalytic nitrogen fixation using electrocatalysts has attracted the most intense investigative attention from the research world, benefitting from the ambient operating conditions and the utilization of electricity produced from renewable energy like wind energy, solar energy, *etc.*[3–5] Moreover, electrochemical catalysis can be easily controlled by adjusting the reaction's temperature and potential to get the desired product. However, electrochemical methods are largely hampered by the high overpotential and low selectivity due to sluggish kinetics and the competitive HER.[6] To circumvent these issues, it is highly recommended to develop active and stable electrocatalysts to enhance NRR activity while suppressing the accompanying HER. In the recent past, extensive research has been undertaken to explore the catalytic activities of potential NRR electrocatalysts including noble metals,[7–9] transition-metal based materials[10–15] and non-metallic materials.[16–18] Transition metal-based nitrides, as well as sulphides, were also predicted to be promising for nitrogen fixation.[19–22] Moreover, efforts are also being undertaken to further optimize their NRR activity by introducing dopants/vacancies,[14,23–30] and modifying the catalyst's morphology/size.[31–35]

Centre for Materials Science and School of Chemistry and Physics, Queensland University of Technology, Gardens Point Campus, QLD 4001, Brisbane. E-mail: aijun.du@qut.edu.au

Single-atom alloys (SAAs) have recently gained momentum towards the design of extremely selective and active catalysts for the production of desired products.[36–40] Substantial work has been done in the area of SAAs particularly on selective hydrogenation[41–43] and H_2 activation.[44] Recently, it was found that an alloy of Pd supported by Cu(111) displayed an excellent activity towards the dissociation of H_2.[45] Tierney *et al.* later found that such alloys also promoted the spillover of H atoms across the surface of the catalyst.[46] Further, Long *et al.* reported a CuPd SAA as a highly selective photocatalyst for converting CO_2 to CH_4. The paired Cu–Pd atoms with tuneable d-band centres enhanced the activity and selectivity of the catalyst. Although SAAs have been shown to catalyze C–O coupling, NO reduction, CO oxidation, hydrogenations, and dehydrogenations,[39] not much has been done in the field of electrocatalytic reduction of nitrogen.[47] Inspired by this strategy, we proposed SAAs based on Ru(0001) to boost their catalytic activity towards nitrogen fixation.

Ruthenium (Ru)-based catalysts have been extensively studied, both computationally and experimentally, for the NRR and have been found to exhibit good performance.[9,48–58] Skúlason *et al.* in 2011 studied the free energy profile of flat Ru(0001) for the nitrogen reduction reaction.[59] They reported a free energy change of 1.08 eV for the potential determining step (PDS). However, in another study by Tayyebi *et al.*, the free energy change for the PDS was found to be 0.80 eV, suggesting poor activity of flat Ru(0001) for efficient NRR.[53] In our work, we systematically investigated the feasibility of SAAs based on TM@Ru(0001) for efficient NRR by examining their stability, activity and selectivity. We performed a number of systematic DFT calculations to investigate the structural stability, adsorption of N_2, minimum energy pathway, free energy change for the PDS, and kinetic barrier for the hydrogenation steps. Out of 20 candidates, we identified Ti@Ru(0001) and V@Ru(0001) as potential candidates based on a series of results obtained from the adsorption energy of the N_2 molecule and the free energy change corresponding to the PDS. Among these, V@Ru(0001) presents enhanced electrocatalytic properties with a very low negative limiting potential of about −0.15 V *vs.* SHE along with an activation barrier of 1.14 eV. Indeed, many researchers have found that vanadium as a dopant could increase the activity of the substrate for effective NRR.[60–63] Furthermore, microkinetic modelling was used to calculate the turnover frequency for the V@Ru(0001) catalyst which was found to be 4.24×10^{-3} per s per site for 25% N_2 partial pressure at 100 bar pressure and 700 K temperature, which is excellent as compared to that of the pure Ru(0001). In addition to this, the selectivity and stability of these selected electrocatalysts were studied along with the competitive HER. These results may provide essential guidance for the development of SAA electrocatalysts for ammonia synthesis under mild conditions of temperature and pressure based on ruthenium.

2. Computational details

In this work, a close-packed hcp(0001) surface was used to represent the flat surface of a Ru atom. The Ru(0001) substrate was modelled by a four-layer slab in which the bottom two layers were fixed, and the top two layers were allowed to relax along with the adsorbed moiety to enhance the calculation speed. A vacuum space of 15 Å was employed to decouple the interactions between two adjacent supercells.

All the structure optimizations and the electronic properties calculations were undertaken using the Vienna *Ab initio* Simulation Package (VASP)[64–67] code based on the spin-polarized density functional theory (DFT) approach. The electron correlation functional was considered through the generalized gradient approximation (GGA)[68] in the form of Perdew–Burke–Ernzerhof (PBE). The projector augmented wave (PAW) method[69] was applied to generate the pseudopotentials. The kinetic cut-off energy was set to be 500 eV, while all the self-consistent optimizations were done with thresholds of 1×10^{-5} and 0.001 eV Å^{-1} for energy and force convergence, respectively. In all the calculations, van der Waals interactions were addressed using the DFT+D3 method.[70] An implicit solvation model with water as implemented in VASPsol was used to consider the solvent effect in the reaction.[71] The charge populations were studied using the Bader charge analysis method.[72] The structural stability of the catalyst was evaluated using *ab initio* molecular dynamics (AIMD) simulations.[73] The time step was set to be 1.0 fs, and simulations were conducted at 300 K.

The NRR process was calculated based on the computational hydrogen electrode (CHE) model. The reference potential was set to be that of the standard hydrogen electrode (SHE). The Gibbs free energy change was calculated using the following equation

$$\Delta G = \Delta E_{DFT} + \Delta E_{ZPE} - T\Delta S$$

where ΔE_{DFT} is the total energy difference from DFT calculations, ΔE_{ZPE} is the change of zero-point energy, T is the temperature (298.15 K), and ΔS is the change in entropy of products and reactants. The limiting potential for evaluating the NRR activity was calculated using the equation

$$U_L = -\Delta G_{max}/e$$

where ΔG_{max} is the free energy change corresponding to the PDS. The more negative the value of the limiting potential, the lower the activity of the catalyst.

The climbing-image nudged elastic band (CI-NEB) method[74] was used to calculate the energy barrier for the transition state. Eight images were added in between the initial and final positions for CI-NEB calculations. The intermediate images were optimized until the forces converged to 0.03 eV Å^{-1}. In microkinetic modelling, a quasi-equilibrium approximation was used to study the NRR on V@Ru(0001). The TOF was calculated as the reaction rate for the potential determining step, while all other hydrogenation steps were considered as a fast equilibrium process. All the details for the calculation of TOF are given in the ESI.† Furthermore, to analyze the chemical bonding between the TM and the adsorbate, we used projected crystal orbital Hamilton population[75,76] (pCOHP) analysis as implemented in the LOBSTER code.[77]

3. Results and discussion

The optimized geometry of TM@Ru(0001) SAAs (for example, V@Ru(0001)) is as shown in Fig. 1. One of the atoms from the top layer of bulk Ru(0001) was replaced with a TM (Sc–Zn, Y–Cd), which is expected to enhance the catalytic performance of the pure Ru(0001) due to charge redistribution. A number of different doping sites on the top layer of Ru(0001) were studied, and all the sites were found to be equally favourable and were of the same energy. All the studied TM@Ru(0001) complexes have similar geometry to the one shown in Fig. 1.

3.1 Screening of TMs supported on Ru(0001) as NRR catalysts

The NRR is a very complicated process that can take place through various mechanisms like distal, alternating, enzymatic and consecutive mechanisms, as shown in Fig. 2. Calculating all the intermediates in different mechanisms would cost lots of computational resources; thus, it is very important to frame a strategy to identify promising candidates. In the case of the NRR, the first step involves the N_2 adsorption on the catalyst surface. It has been found that in most of the cases, the protonation of the N_2 molecule to form $*N_2H$ or the last step in which the $*NH_2$ intermediate upon hydrogenation forms $*NH_3$ constitutes the PDS.[59,78–81] The weak interaction of N_2 with the catalyst results in high energy consumption due to the cleavage of the inert $N\equiv N$ bond. On the other hand, in the case of the strong binding of N_2 to the substrate, the last hydrogenation step becomes difficult. Thus, an efficient NRR catalyst should satisfy certain criteria such as (1) ΔG_{N2} should be lower than 0 eV to ensure effective adsorption of N_2 on the surface of the catalyst, (2) ΔG for the first hydrogenation step, ΔG (N_2–NNH), usually corresponding to a rate-determining step should be smaller than 0.50 eV, which is close to the calculated barrier for one of the best electrocatalysts[4,78] and (3) high selectivity of the NRR over the HER.

Based on criterion 1, we screened a number of TM@Ru(0001) (TM = Sc–Zn, Y–Cd) by computing ΔG of N_2 adsorption (Fig. 3(a)). It is clear that Ti, V, Cr, Nb and Tc (green area of

Fig. 3(a)) based SAAs exhibited a suitable Gibbs free change for N_2 adsorption, while some of the SAAs have a positive free energy change, indicating weak adsorption, and the rest of them have a very high negative free energy change. Rh@Ru(0001) is also considered for further analysis as the free energy change for N_2 adsorption is quite close to 0 eV. Following criterion 2 (Fig. 3(b)), the catalytic pathway for Ti@Ru(0001) for side-on adsorption and V@Ru(0001) for both side-on and end-on adsorption is considered for further investigations. The HER is an unwanted competitive reaction with respect to the NRR, and often lowers the catalytic performance of the electrocatalyst. To analyze the reaction selectivity, the adsorption energies of H^+ and N_2 (values are given in Table S1†) are calculated for each of the catalysts via V@Ru(0001) and Ti@Ru(0001) and are found to be highly negative (<1 eV). Strong adsorption would lead to the difficult desorption of H_2 from the catalyst surface, making the competitive HER highly suppressed. It was found that the H* species is preferably adsorbed on the neighbouring Ru atom, leaving the active site vacant for the adsorption of intermediates during the reduction process. The NRR intermediates can be hydrogenated by the adsorbed H* species. In addition, the kinetic barrier for hydrogen formation on V@Ru(0001) and Ti@Ru(0001) was calculated using the CI-NEB method and was found to be 1.70 eV and 1.09 eV, respectively. The calculated kinetic barrier for H_2 formation is higher than the barrier obtained for ammonia formation (1.14 eV), indicating that the HER is suppressed from the kinetic aspect. Thus, based on criterion 3, V@Ru(0001) and Ti@Ru(0001) exhibit high selectivity towards the NRR.

3.2 N_2 adsorption on TM@Ru(0001)

Effective adsorption of N_2 on the surface of the catalyst is of paramount importance for an efficient nitrogen reduction process. It is well known that TMs with empty d-orbitals can strongly interact with the adsorbed N_2 molecule through the formation of a N–metal bond.[5,82] The exceptional performance of TM based catalysts can be attributed to the coexistence of their vacant and filled d-orbitals. The empty d-orbital of the TM can accept electron density from the filled s-favourable orbital
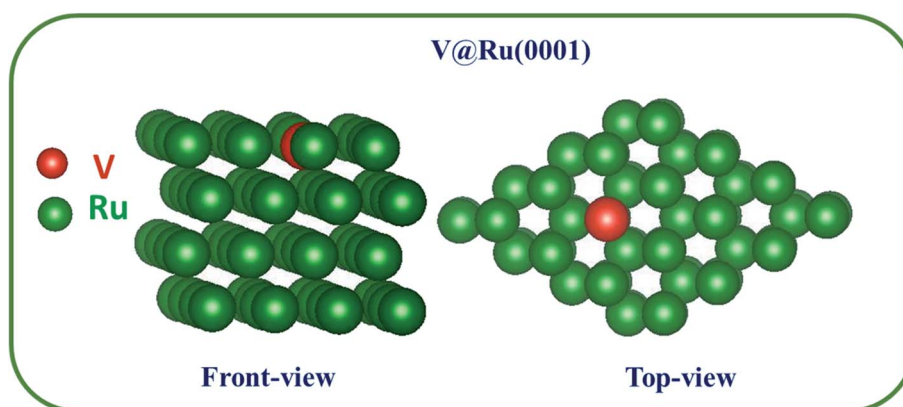

Fig. 1 Optimized structure for V@Ru(0001). Both the front view and top view have been provided. The green and red spheres denote ruthenium (Ru) and vanadium (V) atoms, respectively.
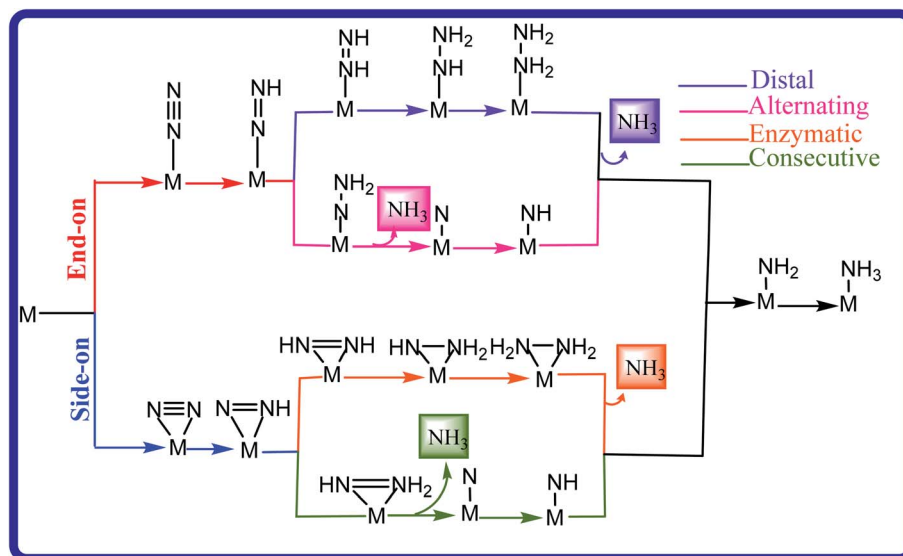
6206 | *J. Mater. Chem. A*, 2022, **10**, 6204–6215

This journal is © The Royal Society of Chemistry 2022

Fig. 2 Systematic illustration of the different mechanisms encountered during the NRR.
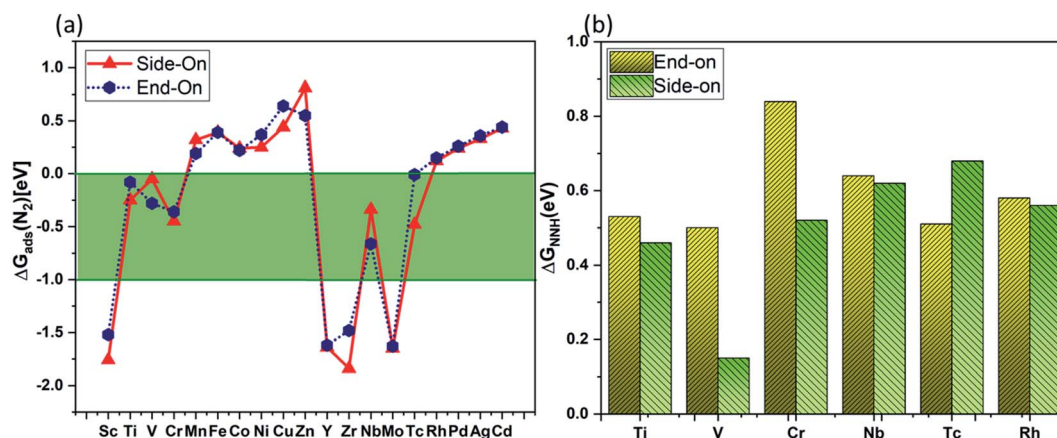

Fig. 3 Screening results of the TM@Ru(0001) system for the NRR process using the (a) free energy change of *N_2 adsorption and (b) the first hydrogenation step of N_2 reduction ΔG_{NNH}. The green shaded portion in (a) corresponds to the acceptable values for the effective adsorption of N_2 on the catalyst's surface.

of the N_2 molecule, while the filled orbital of the TM can donate the electron density to the empty π^* antibonding orbital of the N_2 molecule (Fig. 4a). The "acceptance–back donation" of electrons between the TM and N_2 molecule plays a significant role in the activation of the N_2 molecule.

The adsorption of N_2 on the substrate takes place *via* two common configurations, side-on and end-on, as shown in Fig. 4c and d. In the case of the end-on configuration, only one nitrogen atom binds to the active site, while in the case of the side-on geometry, both the nitrogen atoms of the N_2 molecule form bonds with the active centre. For Ti@Ru(0001), N_2 adsorption prefers the side-on configuration while for the V based complex, the end-on configuration is preferred.

In the case of V@Ru(0001), the N_2 bond undergoes elongation from 1.098 Å (isolated state) to 1.17 Å and 1.13 Å for the side-on and end-on configurations, respectively. The Ti@Ru(0001)

catalyst also displayed similar values for the N≡N elongation. Furthermore, based on the Bader charge difference analysis (Fig. 4b), it was found that 0.56e/0.42e and 0.54e/0.43e charges were transferred from the V and Ti based catalysts to the adsorbed N_2 molecule for side-on/end-on configurations, respectively. All of the above analysis shows that the N≡N bond becomes activated upon adsorption on the surface of the catalyst.

Furthermore, the adsorbed N_2 molecule on the catalyst was further analyzed by using the projected density of states (pDOS) and projected crystal orbital Hamilton population (pCOHP). The pDOS for N_2 adsorption on both pure ruthenium and V@Ru(0001) is depicted in Fig. 5(a) and (b). It is clear that in the case of V@Ru(0001), the π^* orbitals of the adsorbed nitrogen are partially filled, while the antibonding orbitals lie far above the Fermi level in the case of Ru(0001), revealing the active adsorption of N_2 on V@Ru(0001). Further, Fig. 5(c) shows the
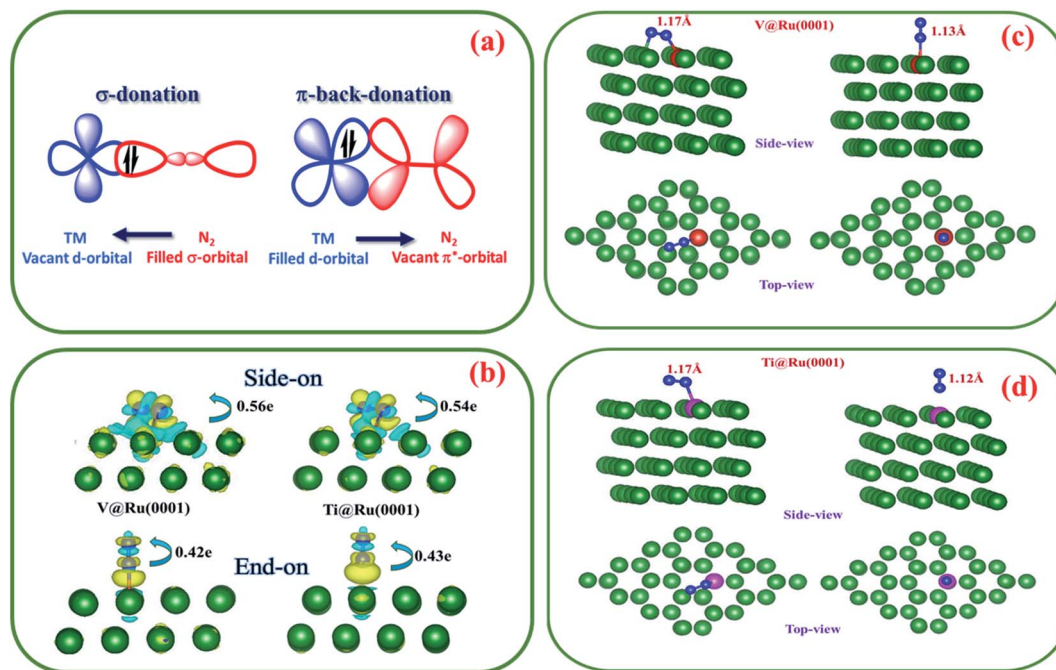
This journal is © The Royal Society of Chemistry 2022

J. Mater. Chem. A, 2022, **10**, 6204–6215 | **6207**

Fig. 4 (a) Schematic demonstration of N$_2$ bonding to a transition metal (TM). (b) The charge density difference of N$_2$ adsorbed on V@Ru(0001) and Ti@Ru(0001) in side-on and end-on configurations with the isosurface value set to 0.001 e Å^{-1}; the yellow and cyan depict positive and negative charges, respectively. (c and d) The side-on and end-on binding of N$_2$ on V@Ru(0001) and Ti@Ru(0001), respectively.

pCOHP analysis in which the bonding contributions are shown on the right and the antibonding interactions are on the left side of the diagram. As predicted by the above figure, the occupied antibonding orbitals of N$_2$ lie near the Fermi level as the bonding states, indicating the adsorption of a N$_2$ molecule on the surface, with the unoccupied π* orbitals above the Fermi level. The integrated COHP (ICOHP) values were calculated by calculating the energy integral up to the highest occupied level. A higher negative value of ICOHP corresponds to an effective binding of N$_2$ on the catalyst. In the case of V@Ru(0001), the ICOHP for end-on adsorption of N$_2$ is −10.91 eV, pointing towards the strong adsorption of N$_2$, which agrees well with the N$_2$ adsorption data for the end-on configuration. Thus, COHP analysis also supports the active adsorption of N$_2$ on the considered materials. The energy difference between 4d (Ru)/2p (N) and 3d (V)/2p (N) in the case of Ru(0001) and V@Ru(0001), respectively, may be responsible for better N$_2$ adsorption on the surface of SAAs, thus showing an increment in their activity for the NRR over pure Ru.

3.3 Stability of TM@Ru(0001)

The stability of TM@Ru(0001) SAAs was investigated using first-principles calculation. It is essential to have strong binding between the TM and the substrate in order to prevent its agglomeration. Thus, we calculated the binding energy E_b between the transition metal and Ru(0001) to analyze its structural stability using the equation $E_b = E_{TM@Ru(0001)} - E_{TM} - E_{Ru(0001)}$, where $E_{TM@Ru(0001)}$, E_{TM} and $E_{Ru(0001)}$ are the energies of the TM@Ru(0001), TM and Ru(0001), respectively. It was found that the binding energies of a single V and Ti on Ru(0001)

were −8.19 eV and −9.31 eV, respectively. Further, the thermodynamical stability of V@Ru(0001) and Ti@Ru(0001) was examined by performing AIMD simulations at 300 K (Fig. S2†). The structures of the catalyst were well maintained, with no notable geometrical buckling even at high temperatures. The negative binding energy and strong thermal stability indicate that Ru(0001) can provide a good anchoring site for the transition metal.

3.4 Electrocatalytic conversion of N$_2$ to NH$_3$ with TM@Ru(0001) (TM = V, Ti) catalysts

3.4.1 NRR using V@Ru(0001). In this section, we discuss the catalytic performance of V@Ru(0001) for the conversion of N$_2$ to NH$_3$ by considering all the possible routes. Due to the similar binding strengths of N$_2$ through side-on and end-on configurations, both the reduction pathways were taken into consideration. As shown in Fig. 2, there are four possible reaction pathways: enzymatic and consecutive for the side-on configuration, and distal and alternating for the end-on configuration in which six elemental proton-coupled electron transfer steps are involved. In the case of enzymatic and alternating reduction pathways, H$^+$/e$^-$ pairs attack the two N atoms alternately, while in consecutive and distal mechanisms, H$^+$/e$^-$ pairs first attack one of the N atoms, converting it to NH$_3$, and then attack the other nitrogen atom to form the second NH$_3$ molecule.

Fig. 6 and 7 show the free-energy diagrams for the reduction of N$_2$ to NH$_3$ through consecutive and enzymatic reaction pathways along with the structures of various reactive intermediates encountered along the reaction pathway, respectively.
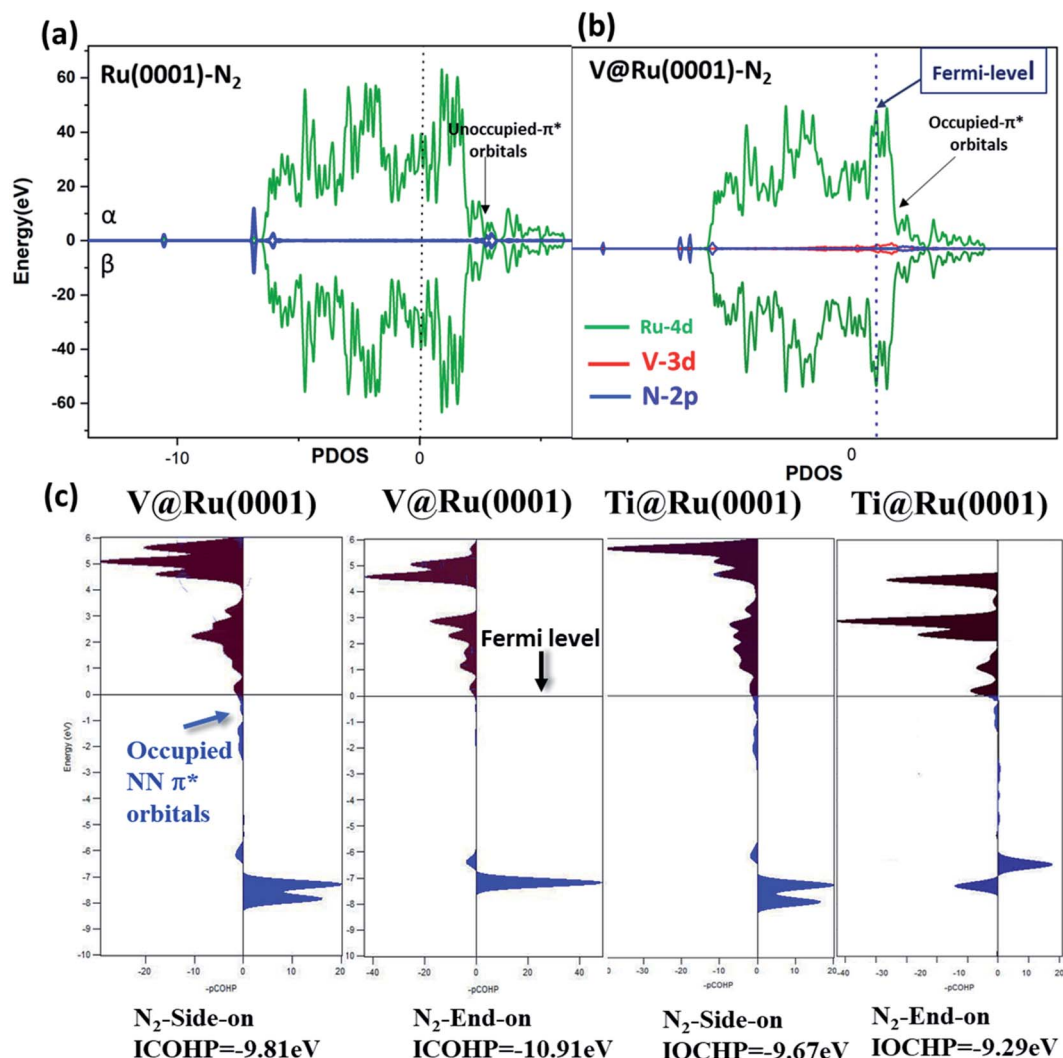
6208 | *J. Mater. Chem. A*, 2022, **10**, 6204–6215

This journal is © The Royal Society of Chemistry 2022

Fig. 5 Partial density of states (PDOS) for (a) nitrogen adsorbed on pure Ru(0001), (b) V@Ru(0001) (c) projected crystal orbital Hamilton population (pCOHP) for N_2 adsorption on V@Ru(0001) and Ti@Ru(0001) in side-on and end-on configurations.

The cartesian coordinates for all the formed intermediates during the reduction process are given in Table S2.† Both these pathways involve six elemental steps of proton-coupled electron transfer to the adsorbed N_2, with the liberation of two NH_3 molecules. The adsorbed N_2 in the side-on configuration reacts with one pair of H^+/e^- to form *N–*NH with an uphill free energy of only 0.15 eV. In the second step, the reactive intermediate, *N–*NH, after reaction with one H^+/e^- pair can either form *N–*NH_2 through a consecutive mechanism with a free energy change of −0.49 eV or can form *NH–*NH following an enzymatic pathway with ΔG of −0.15 eV. In the case of the consecutive reaction pathway, the H^+/e^- pair attacks *N–*NH_2 and forms a *N intermediate along with the release of an NH_3 molecule with a free energy change of −1.47 eV. The formed reactive intermediate after further hydrogenation steps ultimately releases another ammonia molecule accompanied by the liberation of the catalyst. However, in the case of the enzymatic mechanism, *NH–*NH upon reaction with a proton–electron pair forms *NH–*NH_2 with ΔG of −0.40 eV, which on

further reaction produces *NH_2–NH_2 with a free energy change of 0.30 eV. This step corresponds to the potential determining step for the enzymatic pathway. The proton–electron pair attacks *NH_2–NH_2 ($\Delta G = -1.51$ eV) and produces one ammonia molecule along with an *NH_2 reactive species which on further reaction produces another ammonia molecule.

In the case of the consecutive pathway, only the first and the fourth hydrogenation steps were found to be uphill in energy. During the whole reduction process through the consecutive pathway, the potential limiting step is the hydrogenation of *N_2 to *N–*NH with an ultralow limiting potential of only −0.15 V, which is quite low as compared to those of various TM based catalyst for the NRR reported so far.[52,83–85] Similar to the consecutive pathway, the enzymatic pathway also encountered two positive free energy changes during the hydrogenation steps. However, in the latter case, the limiting potential was found to be −0.30 V corresponding to the conversion of *NH–NH_2 to an *NH_2–NH_2 intermediate. The rapid desorption of the formed NH_3 from the surface of the catalyst is important for the
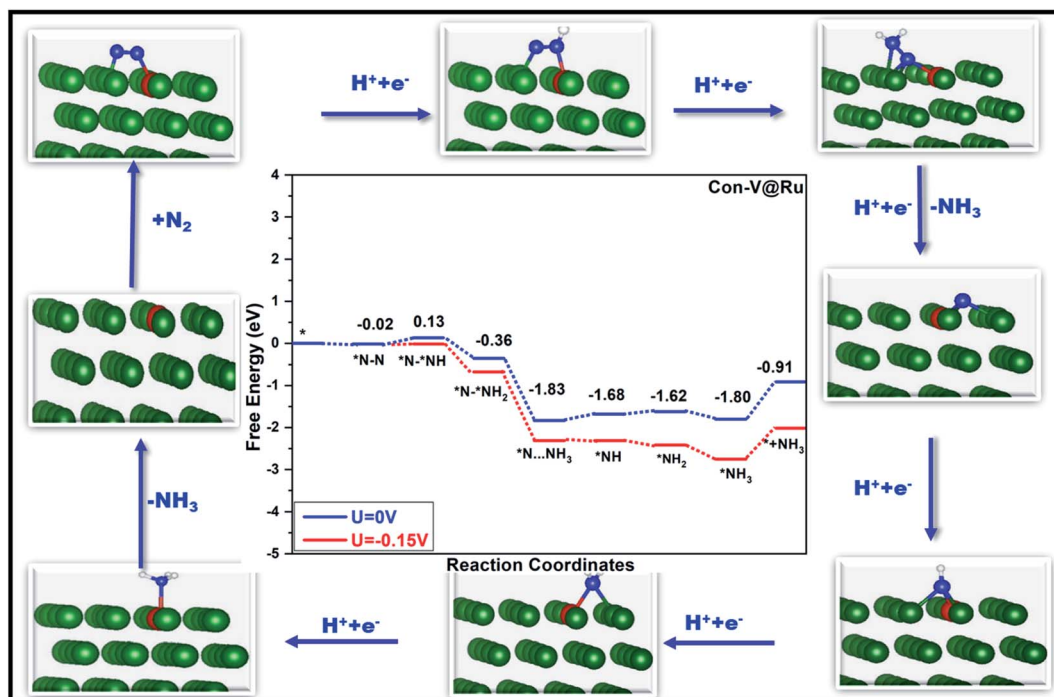
Fig. 6 Free-energy diagram for N_2 reduction *via* a consecutive mechanism at different applied potentials along with the corresponding structures of the intermediates involved in the reduction process. Green, red, blue and white balls represent Ru, V, N and H atoms, respectively.
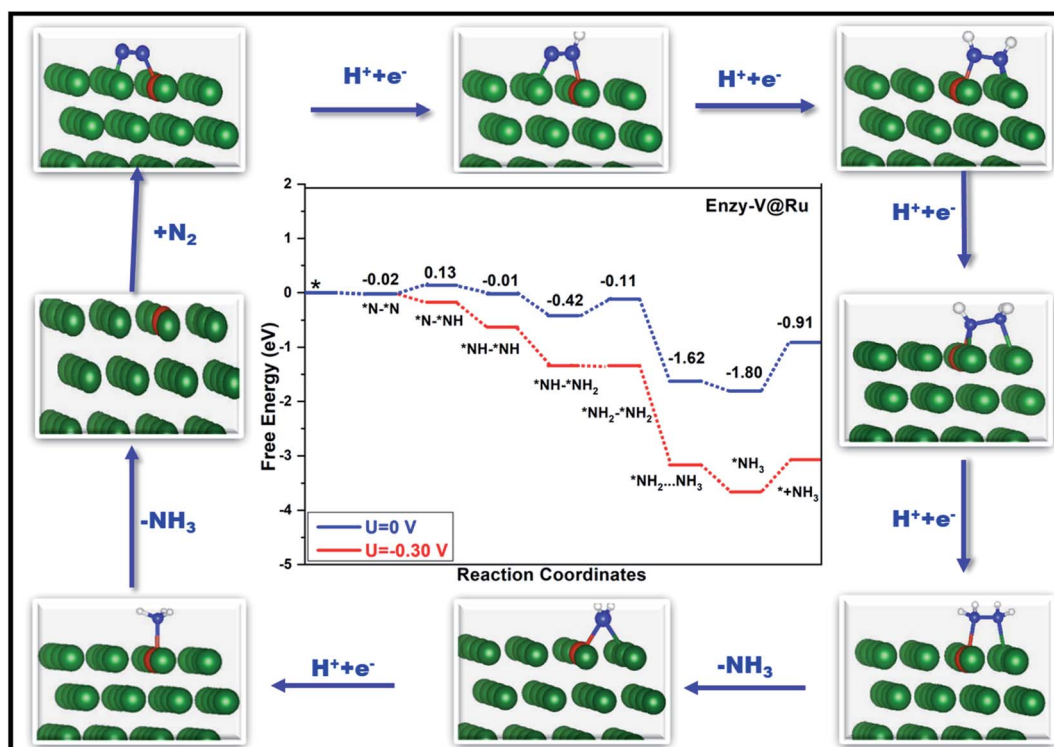

Fig. 7 Free-energy diagram for N_2 reduction *via* an enzymatic mechanism at different applied potentials along with the corresponding structures of the intermediates involved in the reduction process.

6210 | *J. Mater. Chem. A*, 2022, **10**, 6204–6215

This journal is © The Royal Society of Chemistry 2022

regeneration of the active sites which is in turn good for the catalyst's long durability. The desorption of the produced ammonia is a fast process with a free energy change value of only 0.89 eV, indicating its excellent performance as a catalyst.

In addition to consecutive and enzymatic mechanisms, alternating and distal pathways were also explored for the NRR process. The free energy diagram for each of these pathways with the optimized structures of the reaction intermediates is shown in Fig. S3 and S4,† respectively. In case of the alternating pathway, the H^+/e^- pair attacks the two nitrogens alternatively to generate two molecules of NH_3. However, in the case of the distal mechanism, a H^+/e^- pair first attacks the remote nitrogen to convert it into NH_3 and then the remaining N atom reacts with another H^+/e^- pair to generate another molecule of NH_3. From Fig. S3,† it is clear that the ΔG of N_2 adsorption in the end-on mode is negative ($\Delta G = -0.28$ eV), indicating the spontaneity of the reaction. However, the protonation of $*N_2$ is non-spontaneous with ΔG of 0.50 eV, and this step corresponds to the potential-limiting step for the distal mechanism. In the case of the alternating mechanism, the hydrogenation of $*N–NH$ into $*NH–NH$ is the rate-limiting step with ΔG of 0.89 eV, which is quite high compared to all other pathways.

In addition to the associative pathway, the dissociative pathway was also investigated. The kinetic barrier for the scission of the N_2 bond was calculated using the CI-NEB method and was found to be 1.90 eV which is very high to be achievable under moderate conditions of temperature and pressure.

Thus, for the V@Ru(0001) catalyst, out of the four studied pathways, consecutive and enzymatic mechanisms are the preferred ones showing excellent catalytic activity with record low negative values of limiting potential of -0.15 V and -0.30 V vs. SHE, respectively, for the conversion of N_2 to NH_3. Alternating and distal mechanisms, however, correspond to high negative values of limiting potential.

Lastly, in the case of the V@Ru(0001) catalyst, we calculated the solvation effects on the free energy values for the various hydrogenated steps in the case of the consecutive pathway. An implicit solvent model using water as a solvent was employed, and the calculated free energy diagram for V@Ru(0001) is shown in Fig. S5.† From the figure, it is clear that there is not much effect on the values of the free energy even with the solvent effects. The rate-determining step corresponding to the conversion of $*N_2$ to $*NNH$ is 0.14 eV, which is very close to the value obtained for calculations without the solvent effects. Therefore, no solvation treatment was undertaken for the rest of the calculations.

3.4.2 NRR using the Ti@Ru(0001) catalyst. Ti@Ru(0001) was also studied in detail to elucidate its catalytic behaviour for converting N_2 to NH_3. The free energy change for N_2 adsorption on Ti@Ru(0001) is -0.17 eV (side-on) and -0.08 eV (end-on), indicating that N_2 in the end-on configuration is less effectively adsorbed as compared to the side-on configuration. Moreover, based on Fig. 3b, both alternating and distal pathways for the Ti-based complex would have a high free energy change corresponding to the first hydrogenation step. Thus, we considered only enzymatic and consecutive pathways for N_2 reduction using Ti@Ru(0001) to analyze its catalytic

performance. Fig. S6† presents the free energy diagram for the reduction of N_2 via side-on adsorption along with the corresponding structures of the reaction species formed during the reduction process. The N_2 molecule adsorbed on the catalyst in the side-on configuration captures one pair of H^+/e^- and forms $*N–*NH$ with an energy input of 0.47 eV, together with the elongation of $N{\equiv}N$ from 1.098 Å to 1.17 Å. This step is accompanied by the highest value of $\Delta G = 0.47$ eV during the whole reduction process in both the mechanisms and thus corresponds to the rate-determining step. All the protonation steps except the formation of $*NH_2–NH_2$ ($\Delta G = 0.28$ eV) in the enzymatic pathway and the generation of $*NH$ ($\Delta G = 0.05$ eV) in the consecutive pathway are spontaneous. The last two steps of proton-coupled electron transfer in both mechanisms are common and are thermodynamically favourable. In the case of the Ti@Ru(0001) catalyst, the desorption of the formed $*NH_3$ molecule in the last step shows a slight uphill with a ΔG of 0.51 eV. Thus, the Ti@Ru(0001) catalyst displays good performance with a limiting potential of -0.47 V vs. SHE following the enzymatic pathway as well as the consecutive mechanism.

Furthermore, to obtain deeper insight into the mechanism for both V and Ti-based catalysts, the CI-NEB method was used to calculate the kinetic barrier for each of the steps of the consecutive and enzymatic pathways. The calculated values for the kinetic barrier for each of the hydrogenation steps for the consecutive and enzymatic pathways for the NRR using V@Ru(0001) are given in Tables S3 and S4,† respectively. In the case of the consecutive pathway, the kinetic barrier for the potential determining step is only 1.14 eV which is quite low as compared to that of the pure Ru(0001) surface (1.85 eV).[86] However, for the enzymatic pathway, the energy barrier for the rate-determining step for the conversion of $*NH–NH_2$ to $*NH_2–NH_2$ is 1.51 eV. The activation barrier for the rate-determining step for the consecutive and enzymatic pathways for the Ti@Ru(0001) catalyst is 1.48 eV (Tables S5 and S6†). The calculated activation barrier for H_2 formation is 1.70 eV which is very high as compared to that for the hydrogenation of adsorbed nitrogen to form $*NNH$, and thus the competitive HER process would have a minimal effect on the activity of the V@Ru(0001) for nitrogen reduction.

Thus, based on the above calculations, V@Ru(0001) exhibited improved catalytic activity with a record low negative value of limiting potential of -0.15 V vs. SHE for the conversion of N_2 to NH_3 following the consecutive pathway along with a kinetic barrier of only 1.14 eV for the rate determining step.

3.5 Micro-kinetic modelling

Turnover frequency (TOF) is a measure of the instantaneous efficiency of the catalyst. Thus, microkinetic simulations were employed to evaluate the TOF for the NRR using V@Ru(0001) as a function of temperature and pressure under the quasi-equilibrium approximation.[31] The temperature for this reaction was in the range of 500–1000 K while the pressure was in the range of 1–100 bar.

The contour plot (Fig. 8(a)) gives the variation of TOF with the change of temperature and pressure. It is evident from
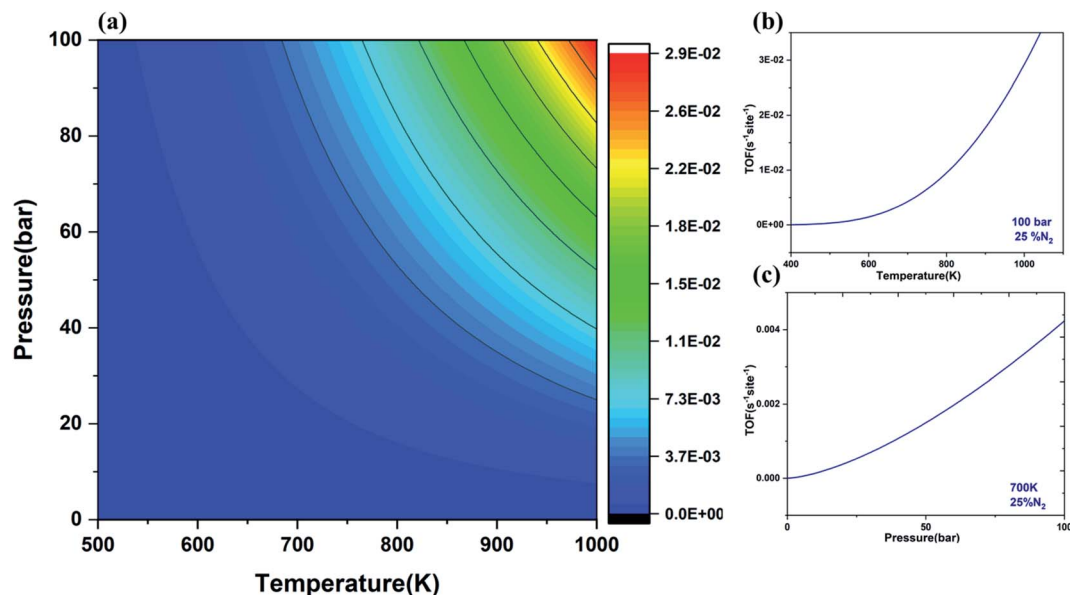
This journal is © The Royal Society of Chemistry 2022

J. Mater. Chem. A, 2022, **10**, 6204–6215 | **6211**

Fig. 8   (a) Contour plot depicting the turnover frequency (TOF) for the formation of NH_3 over the V@Ru(0001) catalyst at various temperatures and pressures with 25% and 75% partial pressures of nitrogen and hydrogen, respectively; (b) graph depicting the variation of temperature with TOF at 100 bar pressure; (c) graph showing the variation of pressure with TOF at 700 K temperature for the V@Ru(0001) catalyst.

Fig. 8(b) and (c) that TOF rises with the rise of temperature and pressure, respectively. The rising temperature help in overcoming the kinetic barrier of the rate-determining step while the increasing pressure can bring more reactant molecules together to react and produce ammonia. The calculated value for the TOF for the formation of NH_3 from N_2 and H_2 using V@Ru(0001) is 4.25×10^{-3} per site per s at 100 bar pressure and 700 K temperature, which is very close to the reported value by Mao *et al.*[86] The obtained value of TOF for the NRR has increased as compared to that of the pure Ru(0001) catalyst (7.04×10^{-5} per site per s). Thus, it can be concluded that SAAs exhibit excellent performance as compared to the pure Ru(0001).

4.   Conclusion

In conclusion, we have undertaken high throughput screening of catalysts based on DFT methods to explore the catalytic performance of 20 single-atom alloys based on transition metal doped Ru(0001) for the NRR. All the 3d and 4d elements (Sc–Zn and Y–Cd) were used as doped atoms on the top layer of Ru(0001), one of the best materials considered so far for the NRR.[49,87,88] In our calculations, it was found that among all the studied catalysts in this work, the V doped Ru(0001) SAA exhibited enhanced NRR activity with a very low negative limiting potential of only -0.15 V *vs.* SHE along with a reduced kinetic barrier of about 1.14 eV corresponding to the rate determining step, following a consecutive pathway for nitrogen reduction. Apart from V@Ru(0001), Ti@Ru(0001) also showed good catalytic performance with a limiting potential of -0.47 V *vs.* SHE for the production of NH_3 *via* enzymatic and consecutive pathways. Both these materials exhibited good thermodynamical stability, selectivity and catalytic activity for the NRR

process. Alloying of Ru with a transition metal helped in tuning the binding energy of the adsorbed nitrogen on the surface of the catalyst, thereby increasing its catalytic activity. SAAs seem to be favourable for decreasing the energy barrier by enhancing the binding strength of nitrogen. This work could possibly encourage more experimental and computational studies towards the design of highly efficient single atom alloys for the electrochemical conversion of N_2 to NH_3.

Conflicts of interest

There are no conflicts to declare.

Acknowledgements

References

1 V. Rosca, M. Duca, M. T. de Groot and M. T. M. Koper, Nitrogen Cycle Electrocatalysis, *Chem. Rev.*, 2009, **109**, 2209–2244.
2 A. Vojvodic, A. J. Medford, F. Studt, F. Abild-Pedersen, T. S. Khan, T. Bligaard and J. K. Nørskov, Exploring the

6212 | *J. Mater. Chem. A*, 2022, **10**, 6204–6215

This journal is © The Royal Society of Chemistry 2022

limits: a low-pressure, low-temperature Haber–Bosch process, *Chem. Phys. Lett.*, 2014, **598**, 108–112.

3 K. C. MacLeod and P. L. Holland, Recent developments in the homogeneous reduction of dinitrogen by molybdenum and iron, *Nat. Chem.*, 2013, **5**, 559–565.

4 Z. W. Seh, J. Kibsgaard, C. F. Dickens, I. Chorkendorff, J. K. Nørskov and T. F. Jaramillo, Combining theory and experiment in electrocatalysis: insights into materials design, *Science*, 2017, **355**, eaad4998.

5 C. Guo, J. Ran, A. Vasileff and S.-Z. Qiao, Rational design of electrocatalysts and photo(electro)catalysts for nitrogen reduction to ammonia (NH$_3$) under ambient conditions, *Energy Environ. Sci.*, 2018, **11**, 45–56.

6 G.-F. Chen, S. Ren, L. Zhang, H. Cheng, Y. Luo, K. Zhu, L.-X. Ding and H. Wang, Advances in Electrocatalytic N$_2$ Reduction—Strategies to Tackle the Selectivity Challenge, *Small Methods*, 2019, **3**, 1800337.

7 M. Nazemi and M. A. El-Sayed, Electrochemical Synthesis of Ammonia from N$_2$ and H$_2$O under Ambient Conditions Using Pore-Size-Controlled Hollow Gold Nanocatalysts with Tunable Plasmonic Properties, *J. Phys. Chem. Lett.*, 2018, **9**, 5160–5166.

8 H. Xie, Q. Geng, X. Zhu, Y. Luo, L. Chang, X. Niu, X. Shi, A. M. Asiri, S. Gao, Z. Wang and X. Sun, PdP$_2$ nanoparticles–reduced graphene oxide for electrocatalytic N$_2$ conversion to NH$_3$ under ambient conditions, *J. Mater. Chem. A*, 2019, **7**, 24760–24764.

9 R. Zhao, C. Liu, X. Zhang, X. Zhu, P. Wei, L. Ji, Y. Guo, S. Gao, Y. Luo, Z. Wang and X. Sun, An ultrasmall Ru$_2$P nanoparticles–reduced graphene oxide hybrid: an efficient electrocatalyst for NH$_3$ synthesis under ambient conditions, *J. Mater. Chem. A*, 2020, **8**, 77–81.

10 W. Gu, Y. Guo, Q. Li, Y. Tian and K. Chu, Lithium Iron Oxide (LiFeO$_2$) for Electroreduction of Dinitrogen to Ammonia, *ACS Appl. Mater. Interfaces*, 2020, **12**, 37258–37264.

11 Y. Liu, Y. Luo, Q. Li, J. Wang and K. Chu, Bimetallic MnMoO$_4$ with dual-active-centers for highly efficient electrochemical N$_2$ fixation, *Chem. Commun.*, 2020, **56**, 10227–10230.

12 H. Nan, Y. Liu, Q. Li, P. Shen and K. Chu, A Janus antimony sulfide catalyst for highly selective N$_2$ electroreduction, *Chem. Commun.*, 2020, **56**, 10345–10348.

13 P. Shen, Y. Liu, Q. Li and K. Chu, FeVO$_4$ porous nanorods for electrochemical nitrogen reduction: contribution of the Fe$_2$C–V$_2$C dimer as a dual electron-donation center, *Chem. Commun.*, 2020, **56**, 10505–10508.

14 T. Wu, H. Zhao, X. Zhu, Z. Xing, Q. Liu, T. Liu, S. Gao, S. Lu, G. Chen, A. M. Asiri, Y. Zhang and X. Sun, Identifying the Origin of Ti^{3+} Activity toward Enhanced Electrocatalytic N$_2$ Reduction over TiO$_2$ Nanoparticles Modulated by Mixed-Valent Copper, *Adv. Mater.*, 2020, **32**, 2000299.

15 T. Xu, D. Ma, C. Li, Q. Liu, S. Lu, A. M. Asiri, C. Yang and X. Sun, Ambient electrochemical NH$_3$ synthesis from N$_2$ and water enabled by ZrO$_2$ nanoparticles, *Chem. Commun.*, 2020, **56**, 3673–3676.

16 Y. Tian, D. Xu, K. Chu, Z. Wei and W. Liu, Metal-free N, S co-doped graphene for efficient and durable nitrogen reduction reaction, *J. Mater. Sci.*, 2019, **54**, 1–10.

17 L. Xia, J. Yang, H. Wang, R. Zhao, H. Chen, W. Fang, A. M. Asiri, F. Xie, G. Cui and X. Sun, Sulfur-doped graphene for efficient electrocatalytic N$_2$-to-NH$_3$ fixation, *Chem. Commun.*, 2019, **55**, 3371–3374.

18 K. Chu, Q.-q. Li, Y.-p. Liu, J. Wang and Y.-h. Cheng, Filling the Nitrogen Vacancies with Sulphur Dopants in Graphitic C$_3$N$_4$ for Efficient and Robust Electrocatalytic Nitrogen Reduction, *Appl. Catal., B*, 2020, **267**, 118693.

19 Y. Abghoui, S. B. Sigtryggsson and E. Skúlason, Biomimetic Nitrogen Fixation Catalyzed by Transition Metal Sulfide Surfaces in an Electrolytic Cell, *ChemSusChem*, 2019, **12**, 4265–4273.

20 M. Gudmundsson, V. Ellingsson, E. Skúlason and Y. Abghoui, Optimizing Nitrogen Reduction Reaction on Nitrides: A Computational Study on Crystallographic Orientation, *Top. Catal.*, 2021, 1–10.

21 H. Li, Y. Liu, K. Chen, J. T. Margraf, Y. Li and K. Reuter, Subgroup Discovery Points to the Prominent Role of Charge Transfer in Breaking Nitrogen Scaling Relations at Single-Atom Catalysts on VS$_2$, *ACS Catal.*, 2021, **11**, 7906–7914.

22 H. Shen, C. Choi, J. Masa, X. Li, J. Qiu, Y. Jung and Z. Sun, Electrochemical ammonia synthesis: mechanistic understanding and catalyst design, *Chem*, 2021, **7**, 1708–1754.

23 Y.-p. Liu, Y.-b. Li, H. Zhang and K. Chu, Boosted Electrocatalytic N$_2$ Reduction on Fluorine-Doped SnO$_2$ Mesoporous Nanosheets, *Inorg. Chem.*, 2019, **58**, 10424–10431.

24 T. Wang, L. Xia, J.-J. Yang, H. Wang, W.-H. Fang, H. Chen, D. Tang, A. M. Asiri, Y. Luo, G. Cui and X. Sun, Electrocatalytic N$_2$-to-NH$_3$ conversion using oxygen-doped graphene: experimental and theoretical studies, *Chem. Commun.*, 2019, **55**, 7502–7505.

25 X.-h. Wang, J. Wang, Y.-b. Li and K. Chu, Nitrogen-Doped NiO Nanosheet Array for Boosted Electrocatalytic N$_2$ Reduction, *ChemCatChem*, 2019, **11**, 4529–4536.

26 K. Chu, Y.-p. Liu, Y.-h. Cheng and Q.-q. Li, Synergistic boron-dopants and boron-induced oxygen vacancies in MnO$_2$ nanosheets to promote electrocatalytic nitrogen reduction, *J. Mater. Chem. A*, 2020, **8**, 5200–5208.

27 K. Chu, J. Wang, Y.-p. Liu, Q.-q. Li and Y.-l. Guo, Mo-doped SnS$_2$ with enriched S-vacancies for highly efficient electrocatalytic N$_2$ reduction: the critical role of the Mo–Sn–Sn trimer, *J. Mater. Chem. A*, 2020, **8**, 7117–7124.

28 Q. Li, Y. Guo, Y. Tian, W. Liu and K. Chu, Activating VS$_2$ basal planes for enhanced NRR electrocatalysis: the synergistic role of S-vacancies and B dopants, *J. Mater. Chem. A*, 2020, **8**, 16195–16202.

29 Y.-b. Li, Y.-p. Liu, J. Wang, Y.-l. Guo and K. Chu, Plasma-engineered NiO nanosheets with enriched oxygen vacancies for enhanced electrocatalytic nitrogen fixation, *Inorg. Chem. Front.*, 2020, **7**, 455–463.

30 C. Fu, Y. Li and H. Wei, Double boron atom-doped graphdiynes as efficient metal-free electrocatalysts for nitrogen reduction into ammonia: a first-principles study, *Phys. Chem. Chem. Phys.*, 2021, **23**, 17683–17692.

This journal is © The Royal Society of Chemistry 2022

J. Mater. Chem. A, 2022, **10**, 6204–6215 | **6213**

31 K. Chu, Y.-p. Liu, Y.-b. Li, H. Zhang and Y. Tian, Efficient electrocatalytic N$_2$ reduction on CoO quantum dots, *J. Mater. Chem. A*, 2019, **7**, 4389–4394.

32 K. Chu, Y.-p. Liu, J. Wang and H. Zhang, NiO Nanodots on Graphene for Efficient Electrochemical N$_2$ Reduction to NH$_3$, *ACS Appl. Energy Mater.*, 2019, **2**, 2288–2295.

33 Y.-p. Liu, Y.-b. Li, D.-j. Huang, H. Zhang and K. Chu, ZnO Quantum Dots Coupled with Graphene toward Electrocatalytic N$_2$ Reduction: Experimental and DFT Investigations, *Chem.–Eur. J.*, 2019, **25**, 11933–11939.

34 K. Chu, Y.-h. Cheng, Q.-q. Li, Y.-p. Liu and Y. Tian, Fe-doping induced morphological changes, oxygen vacancies and Ce^{3+}–Ce^{3+} pairs in CeO$_2$ for promoting electrocatalytic nitrogen fixation, *J. Mater. Chem. A*, 2020, **8**, 5865–5873.

35 K. Chu, H. Nan, Q. Li, Y. Guo, Y. Tian and W. Liu, Amorphous MoS$_3$ enriched with sulfur vacancies for efficient electrocatalytic nitrogen reduction, *J. Energy Chem.*, 2021, **53**, 132–138.

36 G. Kyriakou, M. B. Boucher, A. D. Jewell, E. A. Lewis, T. J. Lawton, A. E. Baber, H. L. Tierney, M. Flytzani-Stephanopoulos and E. C. Sykes, Isolated metal atom geometries as a strategy for selective heterogeneous hydrogenations, *Science*, 2012, **335**, 1209–1212.

37 M. D. Marcinkowski, M. T. Darby, J. Liu, J. M. Wimble, F. R. Lucci, S. Lee, A. Michaelides, M. Flytzani-Stephanopoulos, M. Stamatakis and E. C. H. Sykes, Pt/Cu single-atom alloys as coke-resistant catalysts for efficient C–H activation, *Nat. Chem.*, 2018, **10**, 325–332.

38 J. Liu, M. B. Uhlman, M. M. Montemore, A. Trimpalis, G. Giannakakis, J. Shan, S. Cao, R. T. Hannagan, E. C. H. Sykes and M. Flytzani-Stephanopoulos, Integrated Catalysis-Surface Science-Theory Approach to Understand Selectivity in the Hydrogenation of 1-Hexyne to 1-Hexene on PdAu Single-Atom Alloy Catalysts, *ACS Catal.*, 2019, **9**, 8757–8765.

39 R. T. Hannagan, G. Giannakakis, M. Flytzani-Stephanopoulos and E. C. Sykes, Single-Atom Alloy Catalysis, *Chem. Rev.*, 2020, **120**, 12044–12088.

40 R. Réocreux, P. L. Kress, R. T. Hannagan, V. Çinar, M. Stamatakis and E. C. Sykes, Controlling Hydrocarbon (De)Hydrogenation Pathways with Bifunctional PtCu Single-Atom Alloys, *J. Phys. Chem. Lett.*, 2020, **11**, 8751–8757.

41 F. R. Lucci, J. Liu, M. D. Marcinkowski, M. Yang, L. F. Allard, M. Flytzani-Stephanopoulos and E. C. Sykes, Selective hydrogenation of 1,3-butadiene on platinum–copper alloys at the single-atom limit, *Nat. Commun.*, 2015, **6**, 8550.

42 F. R. Lucci, M. T. Darby, M. F. G. Mattera, C. J. Ivimey, A. J. Therrien, A. Michaelides, M. Stamatakis and E. C. H. Sykes, Controlling Hydrogen Activation, Spillover, and Desorption with Pd–Au Single-Atom Alloys, *J. Phys. Chem. Lett.*, 2016, **7**, 480–485.

43 M. D. Marcinkowski, J. Liu, C. J. Murphy, M. L. Liriano, N. A. Wasio, F. R. Lucci, M. Flytzani-Stephanopoulos and E. C. H. Sykes, Selective Formic Acid Dehydrogenation on Pt–Cu Single-Atom Alloys, *ACS Catal.*, 2017, **7**, 413–420.

44 F. R. Lucci, M. D. Marcinkowski, T. J. Lawton and E. C. H. Sykes, H$_2$ Activation and Spillover on Catalytically Relevant Pt–Cu Single Atom Alloys, *J. Phys. Chem. C*, 2015, **119**, 24351–24357.

45 Q. Fu and Y. Luo, Active Sites of Pd-Doped Flat and Stepped Cu(111) Surfaces for H$_2$ Dissociation in Heterogeneous Catalytic Hydrogenation, *ACS Catal.*, 2013, **3**, 1245–1252.

46 H. L. Tierney, A. E. Baber, J. R. Kitchin and E. C. Sykes, Hydrogen dissociation and spillover on individual isolated palladium atoms, *Phys. Rev. Lett.*, 2009, **103**, 246102.

47 G. Zheng, Y. Li, X. Qian, G. Yao, Z. Tian, X. Zhang and L. Chen, High-Throughput Screening of a Single-Atom Alloy for Electroreduction of Dinitrogen to Ammonia, *ACS Appl. Mater. Interfaces*, 2021, **13**, 16336–16344.

48 M. Kitano, S. Kanbara, Y. Inoue, N. Kuganathan, P. V. Sushko, T. Yokoyama, M. Hara and H. Hosono, Electride support boosts nitrogen dissociation over ruthenium catalyst and shifts the bottleneck in ammonia synthesis, *Nat. Commun.*, 2015, **6**, 6731.

49 S. Back and Y. Jung, On the mechanism of electrochemical ammonia synthesis on the Ru catalyst, *Phys. Chem. Chem. Phys.*, 2016, **18**, 9161–9166.

50 Y. Cao, Y. Gao, H. Zhou, X. Chen, H. Hu, S. Deng, X. Zhong, G. Zhuang and J. Wang, Highly Efficient Ammonia Synthesis Electrocatalyst: Single Ru Atom on Naturally Nanoporous Carbon Materials, *Adv. Theory Simul.*, 2018, **1**, 1800018.

51 Z. Geng, Y. Liu, X. Kong, P. Li, K. Li, Z. Liu, J. Du, M. Shu, R. Si and J. Zeng, Achieving a Record-High Yield Rate of 120.9 for N$_2$ Electrochemical Reduction over Ru Single-Atom Catalysts, *Adv. Mater.*, 2018, **30**, 1803498.

52 C. Liu, Q. Li, J. Zhang, Y. Jin, D. R. MacFarlane and C. Sun, Conversion of dinitrogen to ammonia on Ru atoms supported on boron sheets: a DFT study, *J. Mater. Chem. A*, 2019, **7**, 4771–4776.

53 E. Tayyebi, Y. Abghoui and E. Skúlason, Elucidating the Mechanism of Electrochemical N$_2$ Reduction at the Ru(0001) Electrode, *ACS Catal.*, 2019, **9**, 11137–11145.

54 G.-R. Xu, M. Batmunkh, S. Donne, H. Jin, J.-X. Jiang, Y. Chen and T. Ma, Ruthenium(III) polyethyleneimine complexes for bifunctional ammonia production and biomass upgrading, *J. Mater. Chem. A*, 2019, **7**, 25433–25440.

55 Y. Yao, H. Wang, X.-z. Yuan, H. Li and M. Shao, Electrochemical Nitrogen Reduction Reaction on Ruthenium, *ACS Energy Lett.*, 2019, **4**, 1336–1341.

56 L. Lin, L. Gao, K. Xie, R. Jiang and S. Lin, Ru–polyoxometalate as a single-atom electrocatalyst for N$_2$ reduction to NH$_3$ with high selectivity at applied voltage: a perspective from DFT studies, *Phys. Chem. Chem. Phys.*, 2020, **22**, 7234–7240.

57 A. Liu, M. Gao, Y. Gao, X. Ren, Y. Yang, Q. Yang, Y. Li, L. Gao, X. Liang and T. Ma, DFT study of Ru/graphene as high-performance electrocatalyst for NRR, *Inorg. Chem. Commun.*, 2020, **120**, 108169.

58 A. Liu, M. Gao, X. Ren, F. Meng, Y. Yang, Q. Yang, W. Guan, L. Gao, X. Liang and T. Ma, A two-dimensional Ru@MXene catalyst for highly selective ambient electrocatalytic nitrogen reduction, *Nanoscale*, 2020, **12**, 10933–10938.

59 E. Skúlason, T. Bligaard, S. Gudmundsdóttir, F. Studt, J. Rossmeisl, F. Abild-Pedersen, T. Vegge, H. Jónsson and J. K. Nørskov, A theoretical evaluation of possible transition metal electro-catalysts for N_2 reduction, *Phys. Chem. Chem. Phys.*, 2012, **14**, 1235–1245.

60 M. Zhao, C. Guo, L. Gao, X. Kuang, H. Yang, X. Ma, C. Liu, X. Liu, X. Sun and Q. Wei, Vanadium-doped NiS_2 porous nanospheres with high selectivity and stability for the electroreduction of nitrogen to ammonia, *Inorg. Chem. Front.*, 2021, **8**, 3266–3272.

61 T. Wu, W. Kong, Y. Zhang, Z. Xing, J. Zhao, T. Wang, X. Shi, Y. Luo and X. Sun, Greatly Enhanced Electrocatalytic N_2 Reduction on TiO_2 via V Doping, *Small Methods*, 2019, **3**, 1900356.

62 L. Niu, D. Wang, K. Xu, W. Hao, L. An, Z. Kang and Z. Sun, *Tuning the Performance of Nitrogen Reduction Reaction by Balancing the Reactivity of N2 and the Desorption of NH₃*, Nano Research, 2021.

63 X. Liang, X. Deng, C. Guo and C.-M. L. Wu, Activity origin and design principles for atomic vanadium anchoring on phosphorene monolayer for nitrogen reduction reaction, *Nano Res.*, 2020, **13**, 2925–2932.

64 G. Kresse, From ultrasoft pseudopotentials to the projector augmented-wave method, *Phys. Rev. B*, 1999, **59**, 1758–1775.

65 G. Kresse and J. Furthmüller, Efficiency of *ab initio* total energy calculations for metals and semiconductors using a plane-wave basis set, *Comput. Mater. Sci.*, 1996, **6**, 15–50.

66 G. Kresse and J. Furthmüller, Efficient iterative schemes for *ab initio* total-energy calculations using a plane-wave basis set, *Phys. Rev. B*, 1996, **54**, 11169–11186.

67 G. Kresse and J. Hafner, *Ab initio* molecular dynamics for liquid metals, *Phys. Rev. B*, 1993, **47**, 558–561.

68 J. P. Perdew, K. Burke and M. Ernzerhof, Generalized Gradient Approximation Made Simple, *Phys. Rev. Lett.*, 1996, **77**, 3865–3868.

69 P. E. Blöchl, Projector augmented-wave method, *Phys. Rev. B*, 1994, **50**, 17953–17979.

70 S. Grimme, Semiempirical GGA-type density functional constructed with a long-range dispersion correction, *J. Comput. Chem.*, 2006, **27**, 1787–1799.

71 K. Mathew, R. Sundararaman, K. Letchworth-Weaver, T. A. Arias and R. G. Hennig, Implicit solvation model for density-functional study of nanocrystal surfaces and reaction pathways, *J. Chem. Phys.*, 2014, **140**, 084106.

72 G. Henkelman, A. Arnaldsson and H. Jonsson, A Fast and Robust Algorithm for Bader Decomposition of Charge Density, *Comput. Mater. Sci.*, 2006, **36**, 354–360.

73 E. Paquet and H. L. Viktor, Computational Methods for *Ab Initio* Molecular Dynamics, *Adv. Chem.*, 2018, **2018**, 9839641.

74 G. Henkelman, B. P. Uberuaga and H. Jónsson, A climbing image nudged elastic band method for finding saddle points and minimum energy paths, *J. Chem. Phys.*, 2000, **113**, 9901–9904.

75 S. Maintz, V. L. Deringer, A. L. Tchougréeff and R. Dronskowski, Analytic projection from plane-wave and PAW wavefunctions and application to chemical-bonding analysis in solids, *J. Comput. Chem.*, 2013, **34**, 2557–2567.

76 R. Dronskowski and P. E. Bloechl, Crystal orbital Hamilton populations (COHP): energy-resolved visualization of chemical bonding in solids based on density-functional calculations, *J. Phys. Chem.*, 1993, **97**, 8617–8624.

77 S. Maintz, V. L. Deringer, A. L. Tchougréeff and R. Dronskowski, LOBSTER: a tool to extract chemical bonding from plane-wave based DFT, *J. Comput. Chem.*, 2016, **37**, 1030–1035.

78 J. H. Montoya, C. Tsai, A. Vojvodic and J. K. Nørskov, The Challenge of Electrochemical Ammonia Synthesis: A New Perspective on the Role of Nitrogen Scaling Relations, *ChemSusChem*, 2015, **8**, 2180–2186.

79 L. Li, X. Wang, H. Guo, G. Yao, H. Yu, Z. Tian, B. Li and L. Chen, Theoretical Screening of Single Transition Metal Atoms Embedded in MXene Defects as Superior Electrocatalyst of Nitrogen Reduction Reaction, *Small Methods*, 2019, **3**, 1900337.

80 C. Ling, Y. Ouyang, Q. Li, X. Bai, X. Mao, A. Du and J. Wang, A General Two-Step Strategy–Based High-Throughput Screening of Single Atom Catalysts for Nitrogen Fixation, *Small Methods*, 2019, **3**, 1800376.

81 G. Zheng, L. Li, S. Hao, X. Zhang, Z. Tian and L. Chen, Double Atom Catalysts: Heteronuclear Transition Metal Dimer Anchored on Nitrogen-Doped Graphene as Superior Electrocatalyst for Nitrogen Reduction Reaction, *Adv. Theory Simul.*, 2020, **3**, 2000190.

82 C. Ling, X. Niu, Q. Li, A. Du and J. Wang, Metal-Free Single Atom Catalyst for N_2 Fixation Driven by Visible Light, *J. Am. Chem. Soc.*, 2018, **140**, 14161–14168.

83 X. Chen, X. Zhao, Z. Kong, W.-J. Ong and N. Li, Unravelling the electrochemical mechanisms for nitrogen fixation on single transition metal atoms embedded in defective graphitic carbon nitride, *J. Mater. Chem. A*, 2018, **6**, 21941–21948.

84 X. Zhang, A. Chen, Z. Zhang and Z. Zhou, Double-atom catalysts: transition metal dimer-anchored C ₂N monolayers as N_2 fixation electrocatalysts, *J. Mater. Chem. A*, 2018, **6**, 18599–18604.

85 Q. Cui, G. Qin, W. Wang, K. R. Geethalakshmi, A. Du and Q. Sun, Mo-based 2D MOF as a highly efficient electrocatalyst for reduction of N_2 to NH_3: a density functional theory study, *J. Mater. Chem. A*, 2019, **7**, 14510–14518.

86 X. Mao, Z. Gu, C. Yan and A. Du, Unlocking the potential of ruthenium catalysts for nitrogen fixation with subsurface oxygen, *J. Mater. Chem. A*, 2021, **9**, 6575–6582.

87 S. Dahl, A. Logadottir, R. C. Egeberg, J. H. Larsen, I. Chorkendorff, E. Törnqvist and J. K. Nørskov, Role of Steps in N_2 Activation on Ru(0001), *Phys. Rev. Lett.*, 1999, **83**, 1814–1817.

88 Á. Logadóttir and J. K. Nørskov, Ammonia synthesis over a Ru(0001) surface studied by density functional calculations, *J. Catal.*, 2003, **220**, 273–279.

This journal is © The Royal Society of Chemistry 2022

J. Mater. Chem. A, 2022, **10**, 6204–6215 | **6215**